

1 **A New Dynamic Regime in the Kuroshio/Kuroshio Extension and the**
2 **North Pacific Climate System after 2018**

3
4 Bo Qiu^a and Shuiming Chen^a

5 ^a *Department of Oceanography, University of Hawaii at Manoa, Honolulu, Hawaii*

6 Submitted: March 24, 2025; Accepted: September 12, 2025

7 DOI: 10.1175/JCLI-D-25-0167.1

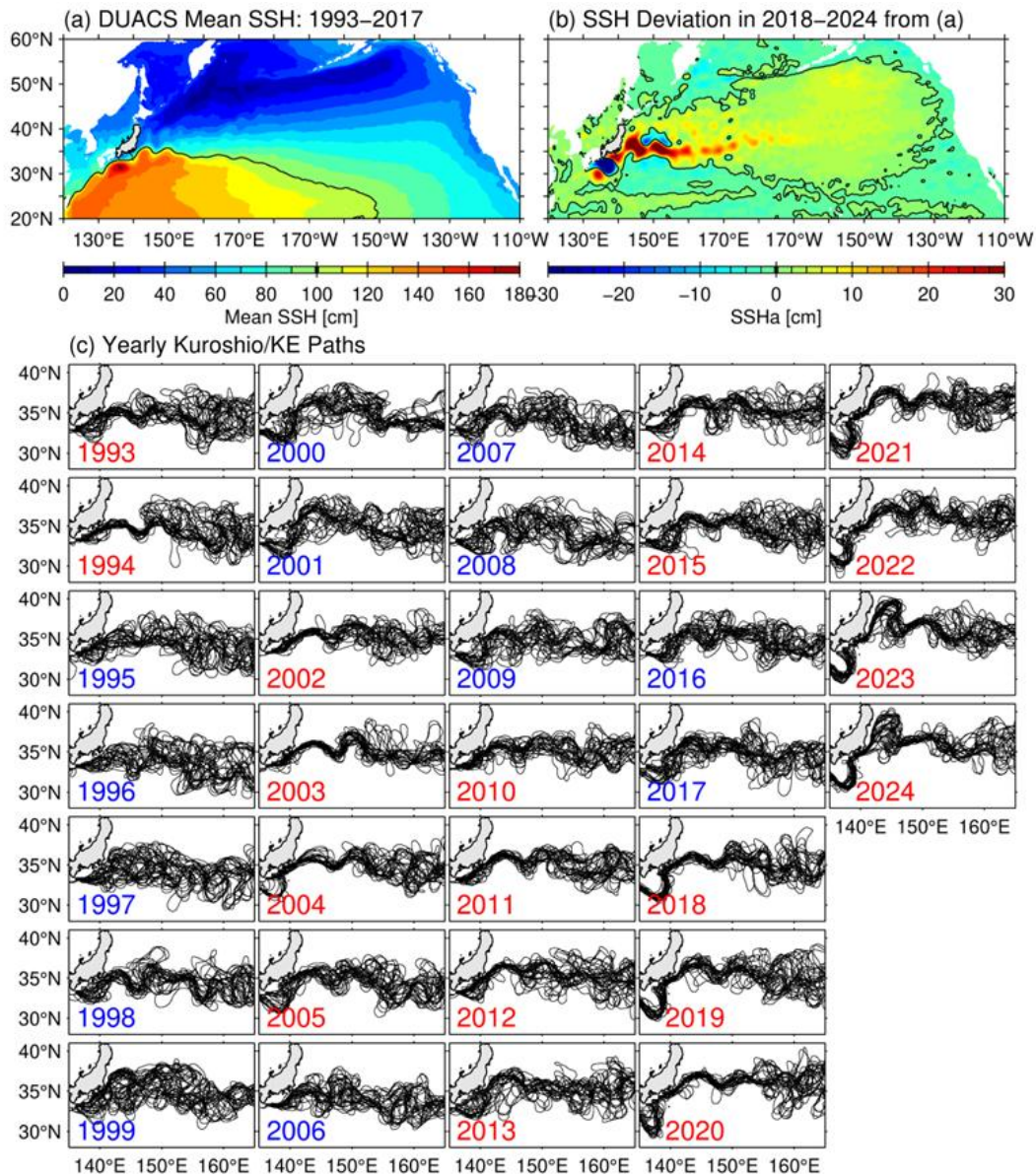
8
9 *Corresponding author:* Bo Qiu, bo@soest.hawaii.edu
10

ABSTRACT

Over the four decades following the 1976/77 climate regime shift, the Kuroshio Extension (KE) in the North Pacific subtropical gyre exhibited quasi-decadal oscillations between stable and unstable dynamic states. These oscillations were facilitated by a delayed negative feedback loop involving wind-forced interior ocean adjustment, its modulation on the KE dynamic state, and the KE's feedback on atmospheric storm tracks and the wind stress field. However, this feedback loop ceased functioning after 2018, giving rise to a new dynamic regime. In this new regime, the Kuroshio south of Japan assumes a persistent large meander (LM) path, while the stabilized KE jet migrates poleward. This study identifies three key processes responsible for the emergence of this regime: (1) a shift in the external forcing field, characterized by intensified wind forcing over the northern subtropical gyre and weakened forcing over the southern gyre; (2) nonlinear reinforcement between the Kuroshio LM and the poleward-migrated KE jet; and (3) altered storm track and wind stress responses to the KE's new stable dynamic state. The establishment of this regime has played a critical role in the recent upper ocean warming – manifested as frequent marine heatwaves – along the 35°–45°N band of the western North Pacific. An upper ocean temperature budget analysis reveals that this cumulative warming is primarily driven by lateral advection associated with the migrating KE jet, while the net surface heat flux forcing acts to dampen the advection-induced temperature anomalies.

1. Introduction

The Kuroshio and its downstream extension, the Kuroshio Extension (KE), form the western boundary current system of the wind-driven North Pacific subtropical gyre (Fig. 1a; Imawaki et al. 2013; Qiu 2019). Due to the coastal and bathymetric constraints, the upstream Kuroshio south of Japan tends to follow one of the two distinct paths: a “non-large meander” path closely hugging the southern Japanese coast, or an offshore detour known as the large meander (LM) path (see Usui et al. 2013, Qiu and Chen 2021, and Hirata et al. 2025b for comprehensive reviews). Upon entering the open North Pacific east of approximately 140°E, the Kuroshio is referred to as the Kuroshio Extension. In this region, free from the topographic constraints, the KE manifests as an eastward-flowing inertial jet characterized by large-amplitude meanders and energetic, pinched-off, eddies (e.g., Mizuno and White 1983). As with other western boundary current systems across the global oceans, the Kuroshio/KE system exhibits the highest levels of eddy variability in the North Pacific.



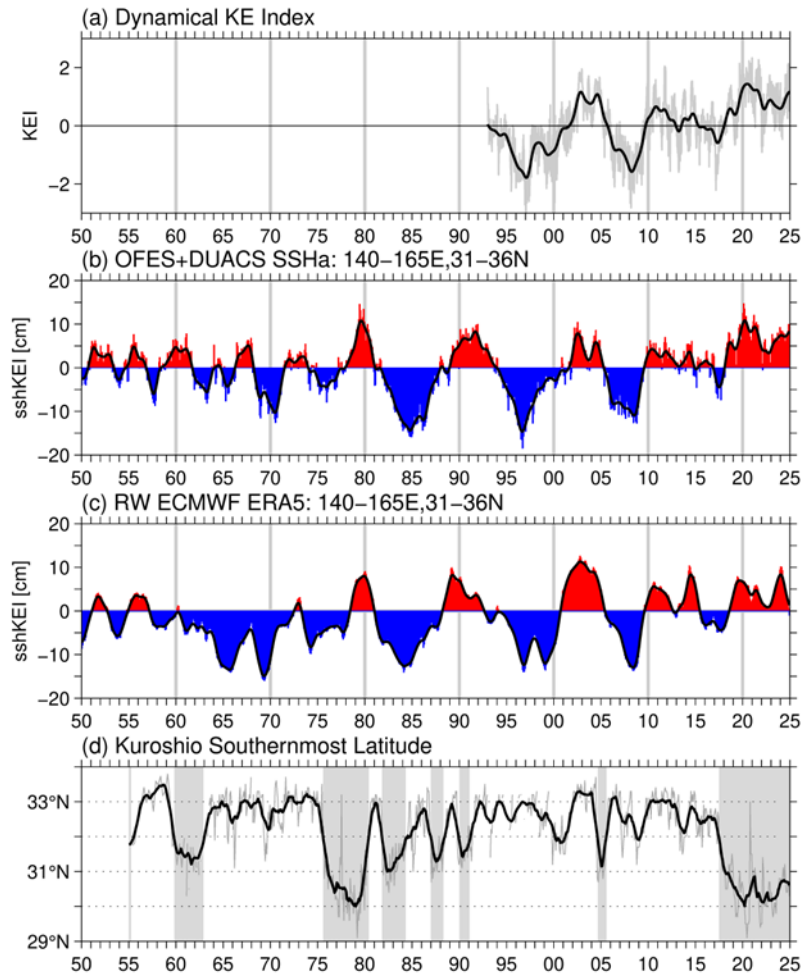
43
 44 Fig. 1. (a) Mean sea surface height (SSH) map of the North Pacific Ocean for the period 1993 – 2017,
 45 based on Jousset et al. (2022). (b) SSH anomaly map for 2018 – 2024, calculated as deviations from the
 46 1993 – 2017 mean SSH field. (c) Yearly trajectories of the Kuroshio and KE, plotted every 14-day
 47 intervals from 1993 onward, derived from satellite altimetry observations [for detailed path derivation
 48 methodology, see Qiu and Chen (2005)]. Red labels indicate years during which the KE predominantly
 49 exhibits a stable dynamic state; blue labels denote years with a predominantly unstable KE state.

50 Historical observations and recent numerical ocean model simulations have shown that the
 51 Kuroshio and KE exhibit fluctuations on interannual to longer timescales, though they typically
 52 vary *independently* (the linear correlation coefficient between the timeseries shown below in
 53 Figs. 2b and 2d for the period prior to 2017 is $R = -0.06$). Satellite altimetry data from the past
 54 32 years reveal that the KE has alternated between stable and unstable dynamic states on

55 decadal timescales, largely in response to surface wind forcing originating from the eastern and
56 central North Pacific basin (Qiu and Chen 2005, 2010; Taguchi et al. 2007; Cebollas et al.
57 2009; Sasaki et al. 2013; Pierini 2014; Joh and Di Lorenzo 2019; Nonaka et al. 2020, among
58 others). During its stable dynamic state (indicated by red years in Fig. 1c), the KE path between
59 140°E to 153°E becomes relatively steady, its eastward transport intensifies, its latitudinal
60 position shifts northward, and the southern recirculation gyre strengthens. In contrast, during
61 the unstable dynamic state (blue years in Fig. 1c), the KE exhibits increased path variability,
62 weaker transport, a southward shift, and a diminished recirculation gyre.

63 Due to their temporal correlations, Qiu et al. (2014) combined the KE path-length, surface
64 transport, latitudinal position, and recirculation gyre strength timeseries into a single metric,
65 referred to as the “KE index”, to concisely quantify low-frequency changes in the KE system
66 (Fig. 2a). In this framework, a positive KE index indicates a stable dynamic state, while a
67 negative index reflects an unstable one. Statistically, the KE index exhibits a strong positive
68 correlation with sea surface height (SSH) anomalies within the KE recirculation region, defined
69 as 31°–36°N and 140°–165°E (cf. Figs. 2a and 2b). It is important to note that the quasi-decadal
70 oscillations between the KE’s stable and unstable states are not confined to the satellite
71 altimetry era. Rather, they appear to have begun following the North Pacific climate regime
72 shift of 1976/77 (Miller et al. 1994; Mantua et al. 1997; Minobe 1997; Mantua and Hare 2002).
73 Before 1976/77, the KE index was predominantly characterized by shorter-period fluctuations
74 in the 4–6-year range. As shown in Figs. 2a–2b, a recent transition occurred in late 2016 and
75 early 2017, when the KE began shifting from a stable to an unstable dynamic state. This
76 transition, however, was reversed in August 2017, coinciding with the onset of a LM in the
77 upstream Kuroshio south of Japan (Sugimoto et al. 2020; Qiu et al. 2020; Joh et al. 2022). As
78 visually evident in Fig. 1c, the KE jet east of Japan has become increasingly stable since 2018,
79 accompanied by a pronounced northward migration of its latitudinal position. Whereas the KE
80 jet’s mean latitude prior to 2018 was around 35°N, it has extended as far north as ~40°N in
81 2023–2024 (Kawakami et al. 2023; Qiu et al. 2023). Simultaneously, the Kuroshio path south
82 of Japan has settled into a persistent LM configuration. In fact, this ongoing LM event is now
83 the longest-lasting in the observational record (see Fig. 2d; Qiu et al. 2023; Hirata et al. 2025b).

84 An inspection of the historical data presented in Figs. 2b and 2d reveals that, while instances
85 of the Kuroshio LM coinciding with a stable KE dynamic state have occurred in the past, the
86 recent concurrence of a highly-stable KE and a persistent Kuroshio LM – lasting over a 7-year
87 period – is *unprecedented*. In light of this newly-emerged Kuroshio/KE dynamic state,



88

89 Fig. 2. (a) KE index derived from the KE's path length, surface transport, latitudinal position, and RG
 90 strength (see Qiu and Chen 2005 for methodology). (b) Timeseries of SSH anomalies in the KE
 91 recirculation gyre box (31° – 36° N, 140° – 165° E), based on DUACS satellite altimetry data for 1993–
 92 2024 and OFES model output for 1950–1992. (c) SSH anomaly timeseries hindcasted using the linear
 93 baroclinic vorticity [Eq. (1)], forced by ERA5 wind stress data. To maintain consistency with panels (a)
 94 and (b), the SSH anomalies are detrended and have a zero mean over the period 1993–2024. (d)
 95 Timeseries of the Kuroshio's southernmost latitude south of Japan (136° – 140° E), as determined by
 96 Japan Meteorological Agency. Shaded periods indicate LM events.

97 numerous recent studies have examined its impacts on regional physical oceanographic
 98 conditions (e.g., Sugimoto et al., 2020; Oka et al., 2021; Nishikawa et al., 2023), as well as on
 99 fisheries, typhoon tracks, and coastal climate variability (e.g., Sugimoto et al., 2021; Lizarbe
 100 Barreto et al., 2021; Oka et al. 2023; Sasaki and Ito 2024; Chang et al. 2025). In contrast,
 101 investigations into the *dynamical processes* that govern this newly established Kuroshio/KE
 102 regime remain limited.

103 The objectives of the present study are threefold. First, we aim to investigate the
104 atmospheric forcing conditions that have contributed to the emergence and persistence of the
105 ongoing new Kuroshio/KE dynamic state. In particular, we emphasize the role of the nonlinear
106 interaction between the Kuroshio and KE, and propose that these interactions have led to the
107 establish of a novel dynamic regime. Second, we examine how the overlying atmosphere across
108 the North Pacific basin responds to this new Kuroshio/KE regime, and how such atmospheric
109 responses may, in turn, feedback to support and maintain the regime. In recent years, a
110 pronounced upper ocean warm anomaly, often referred to as a marine heat wave, has been
111 observed in the western midlatitude North Pacific (e.g., Sato et al. 2024; Kawai et al. 2024;
112 Sugimoto et al. 2025; Minobe 2025). Given the poleward migration by the KE jet from the
113 coast of Japan to as far east as 170°W (see Fig. 1b), it is plausible that this broad-scale warming
114 is dynamically linked to the new Kuroshio/KE regime. At present, a quantitative assessment of
115 this connection remains lacking. Therefore, the third objective of this study is to clarify the
116 dynamical and thermodynamical processes responsible for the recent warming observed in the
117 northwestern Pacific Ocean.

118 This paper is organized as follows. Section 2 describes the satellite altimetry and
119 oceanic/atmospheric reanalysis datasets used in this study. In section 3, we examine the
120 external forcing mechanisms that contribute to the development of the new Kuroshio/KE
121 regime, with particular emphasis on the role of nonlinear interactions between the Kuroshio
122 and KE. Section 4 investigates the potential atmospheric response to this new dynamic regime
123 and explores how such feedbacks may support its persistence. In Section 5, we present results
124 from an upper ocean temperature budget analysis in the North Pacific, focusing on temperature
125 anomalies in the western midlatitude region. Section 6 summarizes the key findings of the
126 study.

127 **2. Observational and reanalysis data**

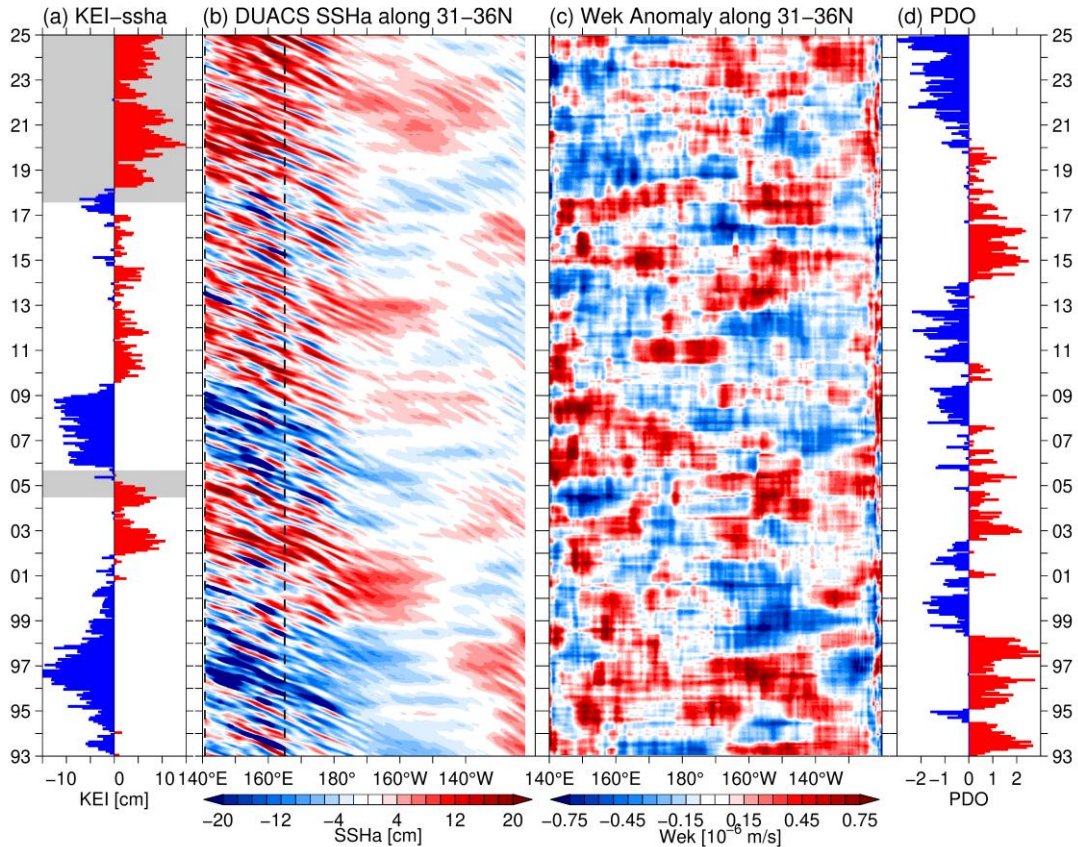
128 To investigate surface circulation and eddy variability, we utilize gridded sea surface height
129 (SSH) data from the Data Unification and Altimeter Combination System (DUACS). The
130 Level-4 DUACS product employs a multi-scale, multivariate optimal interpolation scheme to
131 merge along-track SSH measurements from all available nadir satellite altimeter missions since
132 1993. This dataset provides daily temporal resolution and a spatial resolution of $0.125^\circ \times$
133 0.125° . The data span the period from January 1993 to December 2024.

134 To examine the relationship between oceanic variability and changes in the overlying
135 atmosphere, we use daily reanalysis data from the European Centre for Medium-Range
136 Weather Forecasts (ECMWF) ERA5 product (Hersbach et al. 2020). The ERA5 dataset
137 provides global atmospheric fields at a spatial resolution of $0.25^\circ \times 0.25^\circ$ and covers the period
138 from January 1950 to December 2024. To quantify the amplitude of extratropical storm-track
139 variability, we follow the method proposed by Nakamura et al. (2004), calculating the synoptic-
140 scale (2–8 days) meridional transient eddy temperature flux at the 850-hPa level using hourly
141 ERA5 data.

142 To conduct the upper ocean temperature budget analysis, we use output from the NASA-
143 JPL Estimating the Circulation and Climate of the Ocean Phase II (ECCO2) state estimate
144 (Menemenlis et al. 2008). The ECCO2 model has a horizontal resolution of $0.25^\circ \times 0.25^\circ$ and
145 employs a Green’s function approach to optimize model control parameters such as surface
146 boundary conditions and background eddy viscosity/diffusivity. Because observational data
147 are not directly assimilated into the model’s forward run, ECCO2 maintains dynamic and
148 thermodynamic self-consistency—a condition essential for performing closed heat budget
149 analyses (Wunsch et al. 2009). For this study, we utilize daily ECCO2 outputs spanning from
150 January 1992 to December 2024. To supplement the ECCO2 data, we also employ daily
151 Optimum Interpolation Sea Surface Temperature (OI-SST) data compiled by Huang et al.
152 (2021). The OI-SST dataset provides global SST fields at a spatial resolution of 0.25° and is
153 available from September 1981 to December 2024.

154 **3. A new Kuroshio/KE dynamic regime**

155 In the Introduction, we noted that decadal fluctuations in the KE dynamic state are primarily
156 driven by external wind forcing over the eastern and central North Pacific basin. To investigate
157 how this forced response has evolved in recent years, we present in Fig. 3b the altimeter-
158 derived sea surface height (SSH) anomalies along the 31° – 36° N latitude band—an area that
159 governs the KE dynamic state. Prior to 2017, transitions between the stable and unstable KE
160 dynamic states (Fig. 3a) are clearly linked to the arrival of SSH anomalies originating in the
161 eastern/central North Pacific and propagating into the KE index region (140° – 165° E).
162 Specifically, during the positive phase of the Pacific Decadal Oscillation (PDO; Mantua et al.
163 1997), anomalous positive wind stress curl, or equivalently positive Ekman pumping velocity,
164 in the eastern/central basin enhances Ekman divergence, thereby generating negative SSH
165 anomalies in the 170° – 140° W sector (Figs. 3c–3d). These anomalies propagate westward as



166

167 Fig. 3. (a) Time series of the KE index (identical to Fig. 2b). (b) Time-longitude plot of SSH anomalies
 168 averaged over the 31°–36°N band. Dashed lines indicate the KE recirculation segment (140°–165°E).
 169 To emphasize regional variability, the global mean sea level rise trend of 3.3 mm yr⁻¹ has been removed.
 170 (c) Same as (b), but for the non-seasonal Ekman pumping velocity anomalies W_{ek} , where $W_{ek} = \mathbf{k} \cdot$
 171 $\nabla \times (\boldsymbol{\tau}/\rho_0 f)$ [see Eq. (1)]. (d) PDO index.

172 baroclinic Rossby waves, reaching the KE region after an approximate delay of three years.
 173 Upon arrival, they act to weaken the zonal KE jet, leading to an unstable KE dynamic state
 174 (i.e., a negative KE index). Conversely, when wind stress curl anomalies turn negative during
 175 the negative PDO phase, the resulting westward-propagating positive SSH anomalies reinforce
 176 the KE jet and induce a stable KE dynamic state. Notice that, in addition to the PDO, Tamura
 177 and Tozuka (2023) proposed that the wind forcing relevant to the decadal KE variability could
 178 also arise from atmospheric teleconnections linked to central Pacific El Niño events.

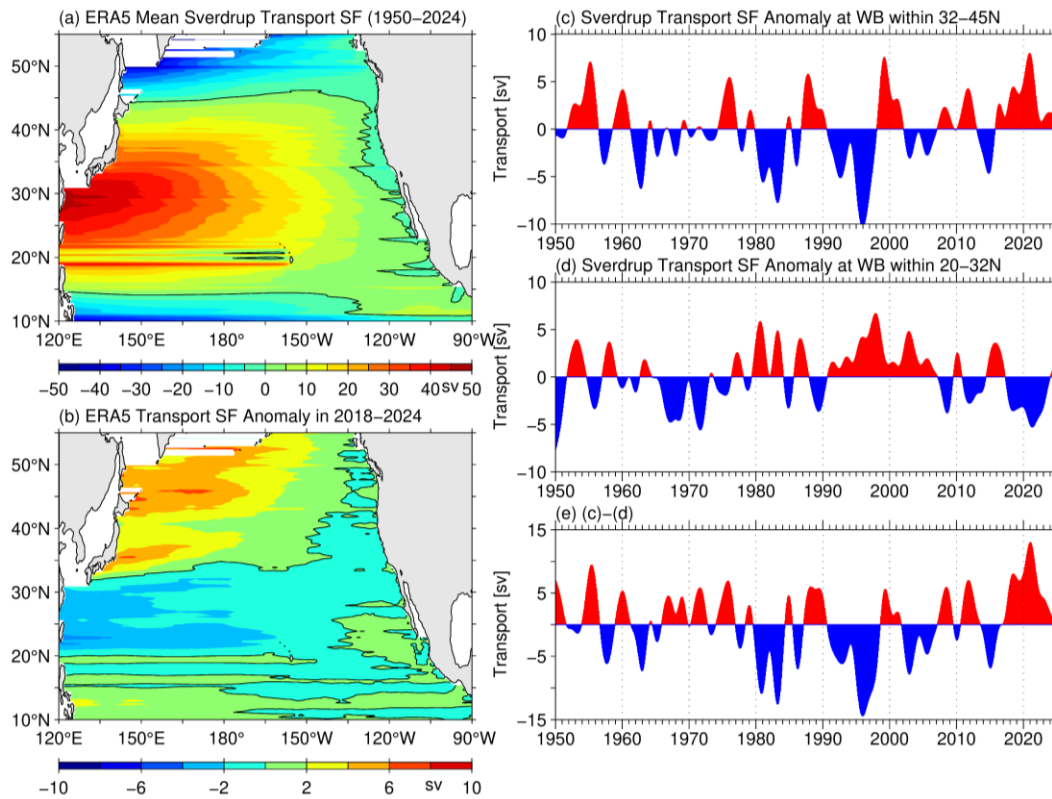
179 However, this forced response of the KE to PDO-phased wind forcing appears to have
 180 changed after 2018. As shown in Fig. 3b, although the wind-driven SSH anomalies over the
 181 central/eastern North Pacific during 2014–2018 were negative—consistent with the positive
 182 PDO phase—these anomalies did not propagate westward into the KE region as would be

183 expected under the delayed Rossby wave mechanism. Instead, the positive SSH anomalies
 184 observed in the western basin during 2018–2022 appear to have originated from local forcing,
 185 specifically from negative wind stress curl anomalies located *west* of the dateline (Fig. 3c).
 186 After 2022, these positive SSH anomalies in the western North Pacific basin persisted and
 187 appear to result from a combination of continued local negative wind stress curl forcing and
 188 incoming positive SSH anomalies from the east, which were generated by the negative PDO-
 189 phased wind forcing over the central/eastern North Pacific. Notice that the importance of
 190 regional wind forcing in modulating KE variability in the North Pacific basin has been
 191 highlighted in a recent study by Fan et al. (2025).

192 Since the Kuroshio path south of Japan entered a LM state in late 2017, it is dynamically
 193 plausible that the SSH value in the KE index box may have been elevated due to the curvature
 194 of the LM south of Japan. According to Sugimoto and Hanawa (2012), when the Kuroshio
 195 adopts a LM path south of Japan, it tends to enter the interior Pacific Ocean through a deep
 196 channel — approximately 2,500-m deep — along the Izu-Ogasawara Ridge, thereby forcing the
 197 upstream KE jet to follow a stable, northerly path. To assess the relative contributions of
 198 surface wind forcing versus the upstream Kuroshio path, we evaluate the SSH changes in the
 199 KE index box (31°–36°N, 140°–165°E) using the ERA5 wind stress data based on the
 200 following wind-forced linear vorticity model in the 1½-layer reduced-gravity upper ocean (e.g.,
 201 Qiu et al. 2014):

$$202 \quad \frac{\partial \eta}{\partial t} - C_R \frac{\partial \eta}{\partial x} = -\frac{g'}{g} \mathbf{k} \cdot \nabla \times \left(\frac{\boldsymbol{\tau}}{\rho_0 f} \right), \quad (1)$$

203 where η is the SSH anomaly, C_R is the long baroclinic Rossby wave speed, g is gravitational
 204 acceleration, g' ($= 0.04 \text{ m s}^{-2}$) is the reduced gravity, f is the Coriolis parameter, ρ_0 is the
 205 reference density, \mathbf{k} is the vertical unit vector, and $\boldsymbol{\tau}$ is the wind stress vector. Note that the
 206 term $\mathbf{k} \cdot \nabla \times (\boldsymbol{\tau}/\rho_0 f)$ on the RHS of Eq. (1) denotes the Ekman pumping velocity (W_{ek}) and the
 207 η evaluated from Eq. (1) reflects only the SSH changes induced by the cumulative wind forcing
 208 east of the KE index box. Figure 2c shows the timeseries of η hindcast by Eq. (1) for the period
 209 1950–2024. The results indicate that the low-frequency SSH variability in the KE index box is
 210 predominantly governed by surface wind forcing across the North Pacific basin. During the
 211 2018–2024 period of our interest, the wind-forced SSH anomalies shown in Fig. 2c explain
 212 75.3% of the variance in the observed SSH anomalies shown Fig. 2b. This proportion is
 213 comparable to the 68.9% variance explained by cross-basin wind forcing during the 1978–2017



214

215 Fig. 4. (a) Sverdrup streamfunction in the North Pacific Ocean based on the 1950–2024 mean surface
 216 wind stress data from ERA5. (b) Anomalous Sverdrup streamfunction for 2018–2024 relative to the
 217 long-term mean in (a). (c) Sverdrup transport anomalies averaged along the northern subtropical gyre
 218 western boundary from 32°N to 45°N. (d) Same as (c), but along the southern subtropical gyre boundary
 219 from 20°N to 32°N. (e) Timeseries of the transport anomaly difference: (c) minus (d).

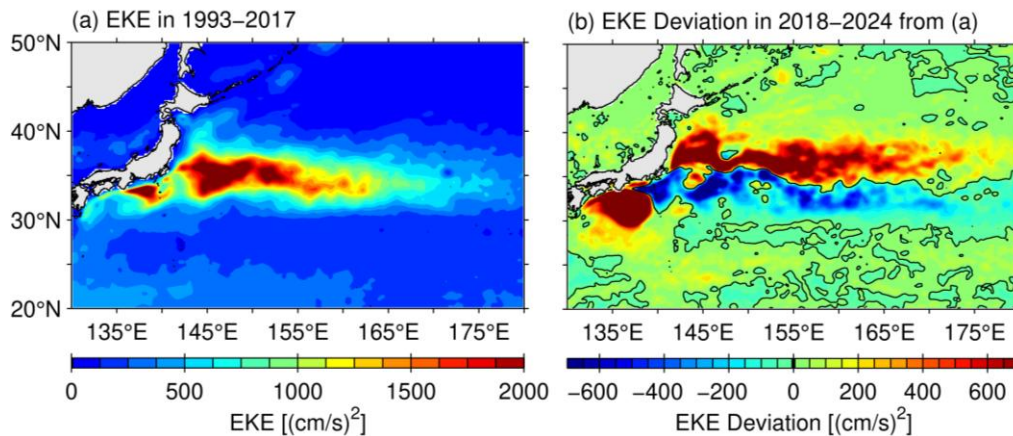
220 period, following the 1976/77 climate regime shift. Assuming a linear response of the KE index
 221 to open-ocean wind forcing and other contributing factors, these results suggest that
 222 approximately one-quarter of the KE index variance arises from non-wind-related influences—
 223 such as upstream control by the persistent LM state of the Kuroshio south of Japan.

224 Given that the Kuroshio and KE are integral components of the wind-driven subtropical
 225 gyre circulation, it is not surprising that variability in wind forcing variability, demonstrated in
 226 Figs. 2b – 2c through the SSH-based KE index, plays a major role. A key question, however,
 227 is what role wind forcing has played in sustaining the unprecedented concurrence of the
 228 persistent Kuroshio LM and the highly stable KE dynamic state observed since 2018. As
 229 indicated in Figs. 2b and 2d, such concurrence has not persisted beyond three years in the past
 230 seven decades. To investigate this issue, we analyze the Sverdrup streamfunction (Ψ_S) across
 231 the North Pacific basin:

232
$$\Psi_S(x, y, t) = \frac{1}{\rho_0 \beta} \int_{x_E}^x \mathbf{k} \cdot \nabla \times \boldsymbol{\tau}(x', y, t) dx', \quad (2)$$

233 where β is the meridional gradient of the Coriolis parameter, and x_E denotes the eastern
 234 boundary longitude. Figure 4a shows the mean Ψ_S map in the North Pacific basin, based on the
 235 ERA5 wind stress data from 1950 to 2024. The wind-driven subtropical gyre, characterized by
 236 positive Ψ_S values, spans approximately from 15°N to 45°N. In Fig. 4b, we plot the Ψ_S anomaly
 237 map in 2018–2024 relative to the long-term mean Ψ_S field. It reveals a distinct dipole structure:
 238 the southern half of the subtropical gyre (20°–32°N) has weakened, while the northern half
 239 (32°–45°N) has strengthened. Although low-frequency fluctuations in the northern and
 240 southern limbs of the gyres have occurred throughout the past 75 years (see Figs. 4c and 4d),
 241 the *concurrent* weakening of the southern gyre and strengthening of the northern gyre sustained
 242 over multiple years is highly unusual (Fig. 4e). In fact, the 2018-2024 period stands out as a
 243 *unique* interval during which this dipole structure persisted continuously for seven years.

244 Dynamically, a weakened southern subtropical gyre implies a reduced inflow of the
 245 Kuroshio south of Japan, a condition confirmed in a recent study by Minobe (2025).
 246 Theoretical and modeling studies have shown that such a weakened inflow favors the
 247 persistence of a LM path due to its β -induced westward drift (White and McCreary 1976; Usui
 248 et al. 2013). In other words, the weakened wind-driven southern subtropical gyre since 2018
 249 has been conducive to sustain the Kuroshio LM south of Japan. In the northern subtropical
 250 gyre north of 35°N, the east coast of Japan near ~141°E serves as the western boundary in the
 251 North Pacific Ocean (see Fig. 4a). As the Sverdrup transport in the northern subtropical gyre
 252 increases after 2018 (Fig. 4c), it has worked to facilitate the poleward migration of the KE jet.
 253 Although these wind-forced changes in the Kuroshio and KE are consistent with the observed
 254 variability since 2018, we argue that the nonlinear interaction between the upstream Kuroshio
 255 LM and the poleward-shifted KE jet has also played an important role in maintaining the on-
 256 going dynamic regime. This argument is supported by the fact that the wind forcing alone
 257 explains only 75.3% of the variance in the observed KE index. A persistent LM forces the
 258 upstream KE jet to veer northeastward, helping push the jet toward higher latitudes. As the KE
 259 jet migrates poleward, its associated mesoscale disturbances also shift poleward. This can be
 260 clearly seen in the DUACS SSH data: as illustrated in Fig. 5, the distribution of eddy kinetic
 261 energy (EKE) after 2018 shows a distinct northward shift, with elevated EKE located north of
 262 35°N when compared to the pre-2018 period. Since the decay of LMs is typically triggered by
 263 incoming mesoscale disturbances from the KE region, a poleward-shifted KE implies fewer



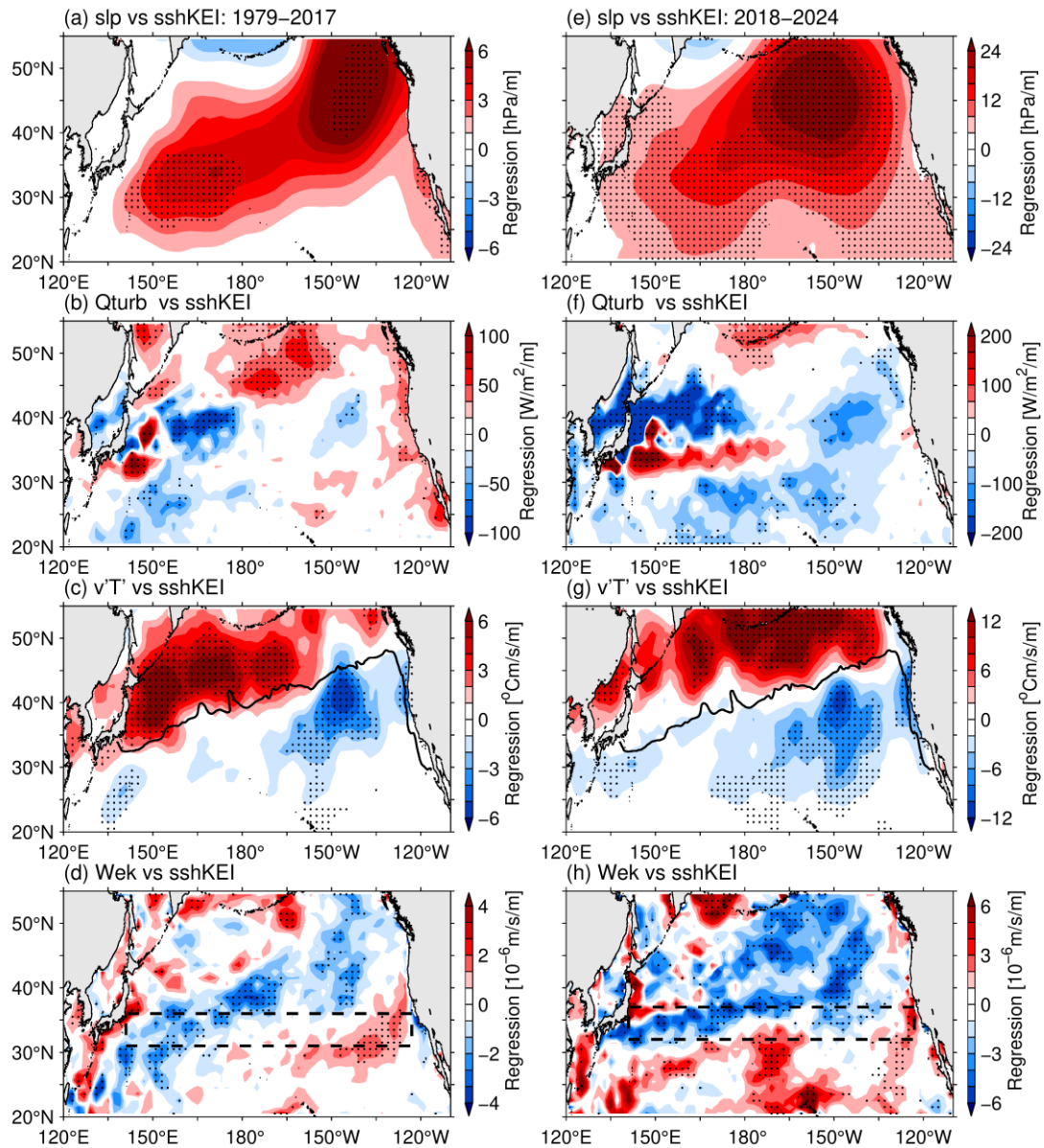
264

265 Fig. 5. (a) Map of eddy kinetic energy (EKE) in the northwestern Pacific Ocean for the period 1993–
 266 2017, calculated from the DUACS SSH data under the geostrophic approximation. (b) EKE anomaly
 267 map for 2018–2024, shown as deviations from the 1993–2017 climatological mean EKE field in (a).

268 eddy perturbations reaching the LM latitudes south of 35°N. This reduced disturbance
 269 enhances the LM’s persistence. We therefore conclude that the persistence of the current
 270 Kuroshio/KE dynamic regime since 2018 results from a combination of the dipolar wind-
 271 forcing anomalies over the subtropical gyre and the mutual reinforcement between the
 272 Kuroshio LM and the poleward-shifted KE jet.

273 4. Midlatitude ocean-atmosphere feedback

274 The Kuroshio and KE transport substantial amounts of warm tropical water poleward,
 275 providing a major source of heat and moisture for the midlatitude atmosphere (Kelly et al.
 276 2010). Numerous studies have demonstrated that this oceanic heat and moisture supply helps
 277 sustain lower-tropospheric baroclinicity, support storm development, and anchor the basin-
 278 wide storm tracks (e.g., Nakamura et al. 2004; Kwon et al. 2013; Taguchi et al. 2012; Small et
 279 al. 2014; Ma et al. 2016; Gan et al. 2023). To explain the quasi-decadal KE dynamic state
 280 oscillations following the 1976/77 North Pacific climate regime shift, Qiu et al. (2014)
 281 proposed a delayed negative feedback mechanism involving interactions between the KE jet
 282 and overlying storm track variability. As shown in Fig. 6b, regression analysis using ERA-5
 283 reanalysis data from 1977 to 2017—lagged by two months relative to the KE index (Fig. 2b)
 284 —reveals enhanced ocean-to-atmosphere surface turbulent heat fluxes over the downstream
 285 KE region during stable dynamic states. The 2-month lag reflects the time required for the
 286 atmospheric response to midlatitude SST anomalies to reach maximum amplitude (Ferreira and
 287 Frankignoul 2005; Deser et al. 2007). Based on high-resolution atmospheric general circulation



288

289 Fig. 6. (a) Regression map of the ERA5 SLP anomaly field against the KE index from 1979 to 2017
 290 (Fig.2b), using a 2-month lag. Black dots indicate areas significant at the 90% confidence level based
 291 on a two-sided Student t -test. (b) Same as (a), but for the surface turbulent heat flux anomaly field
 292 (positive values indicate flux from atmosphere to ocean). (c) Same as (a), but for the 2–8-day band-pass
 293 filtered meridional transient eddy temperature flux anomaly at the 850-hPa level. Thick black line
 294 denotes the time-mean $W_{ek} = 0$ contour. (d) Same as (a), but for the Ekman pumping velocity anomaly
 295 field. Dashed box indicates the region within which Ekman pumping influences the SSH-based KE
 296 index. To isolate extratropical responses, Niño-3.4 signals have been regressed out from all fields in (a)
 297 – (d) prior to the regression analysis. (e) – (h) Same as (a) – (d), but against the KE index during the
 298 2018–2024 period. Due to the poleward migration of the KE jet, the dashed box in (h) is shifted 1°
 299 northward in latitude compared to that in (d).

300 model (AGCM) experiments, Smirnov et al. (2015) demonstrated that this anomalous heat flux
301 forcing can induce deep-reaching ascending motion extending up to the tropopause. With the
302 upward transfer of heat and moisture being balanced by northward transport of nonlinear
303 transient eddies, it works to shift storm tracks poleward and generate a downstream positive
304 sea level pressure (SLP) anomaly across the North Pacific basin (Fig. 6a). This poleward
305 displacement of extratropical storm tracks is further supported by regression analysis of the
306 850-hPa transient eddy flux $\langle v'T' \rangle$ field against the KE index with a two-month lag (see Fig.
307 6c).

308 The mean storm tracks approximately follow the zero Ekman pumping velocity ($W_{ek} = 0$)
309 line, indicated by the black contour in Fig. 6c. This line exhibits a southwest-to-northeast tilt
310 across the North Pacific, shaped by both orographic constraints and diabatic oceanic forcing
311 (Wilson et al. 2009). During stable KE states, storm tracks migrate northward, giving rise to a
312 negative W_{ek} anomaly band that straddles the climatological $W_{ek} = 0$ line (Fig. 6d). South of
313 this band, W_{ek} anomalies become positive due to the northward displacement of wind systems,
314 which brings in weaker negative W_{ek} signals from the southern subtropical gyre. Note that the
315 positive W_{ek} anomalies in the 31° – 36° N band (dashed box in Fig. 6d) of the eastern North
316 Pacific generate local Ekman flux divergence, resulting in negative SSH anomalies. When
317 these wind-induced negative SSH signals propagate westward into the KE region after a delay
318 of ~ 3 years, they weaken the southern recirculation gyre and shift the KE jet southward,
319 allowing it to override the shallow Izu Ridge and transition to an unstable dynamic state.
320 Including both oceanic and atmospheric adjustments, the total time required for this transition
321 is about five years. Once the KE system enters the unstable state, the reverse atmospheric
322 responses depicted in Figs. 6a–6d ensue, eventually prompting a shift back to the stable state.
323 Although the atmospheric response to KE variability is weak compared to internal atmospheric
324 variability, this KE–storm track interaction establishes a delayed negative feedback loop that
325 enhances decadal variability in the extratropical North Pacific ocean–atmosphere system.

326 Based on the ECMWF ERA-Interim reanalysis from 2002 to 2016, Gan et al. (2023)
327 recently found that decadal SST changes in November over the broad KE region (140° – 175° E,
328 30° – 45° N) can induce a basin-wide low SLP anomaly and a southward shift of storm tracks in
329 January over the North Pacific. Their findings differ from those presented in Figs. 6a and 6c.
330 These discrepancies may stem from differences in the study periods and/or the choice of metric
331 — the use of broad-scale SST anomalies in Gan et al. (2023) versus the KE index in our study.

332 Additionally, the focus of Gan et al. (2023) on the atmospheric response in January to
333 November oceanic conditions could contribute to the differing results. As discussed in detail
334 by Taguchi et al. (2012), atmospheric responses to oceanic anomalies can exhibit strong month-
335 to-month variability. In this study, we consider atmospheric responses across all seasons, as
336 ocean–atmosphere interactions occur year-round, and it is the cumulative effect that shapes
337 low-frequency variability in the coupled system. Note that similar basin-wide high SLP
338 responses to decadal KE variability, as shown in Fig. 6a, have also been identified in previous
339 observational and modeling studies, including Frankignoul et al. (2011), Smirnov et al. (2015),
340 Révelard et al. (2016), and Okajima et al. (2018).

341 With the KE system entering a highly stable dynamic state and its axis shifting poleward
342 after 2018, a relevant question arises: Has the KE’s influence upon the overlying atmosphere
343 changed from that in the pre-2018 era? To explore this, we show in Figs. 6e–6h the SLP, surface
344 turbulent heat flux, storm track activity, and Ekman pumping velocity anomalies regressed onto
345 the 2018–2024 KE index with a 2-month lag. Compared to the corresponding regression fields
346 for 1979–2017 (Figs. 6a–6d), broad basin-scale similarities remain, but notable differences
347 emerge. In particular, following the KE’s poleward shift, the associated ocean-to-atmosphere
348 turbulent heat flux anomalies also migrated poleward, as indicated by the negative anomalies
349 in Fig. 6f. In fact, a strong spatial correlation exists between Figs. 6b and 5b, highlighting the
350 close relationship between the KE jet, its associated mesoscale eddies, and their influence on
351 the turbulent heat flux field. This migration of the oceanic heat source is accompanied by a
352 corresponding northward shift in storm track activity (Fig. 6g). The structure of the SLP
353 response also changed: whereas the pre-2018 period featured a quasi-quadrupole pattern (Fig.
354 6a, with a relatively weak southeast negative lobe), the post-2018 pattern is characterized by a
355 more uniform, basin-wide high-pressure anomaly (Fig. 6e). This shift in SLP anomalies is
356 reflected in the Ekman pumping velocity field. The positive W_{ek} anomalies previously seen in
357 the 31°–36°N band of the eastern North Pacific — critical for the negative delayed feedback
358 loop that drives pre-2018 decadal KE oscillations — have been largely replaced by *negative*
359 anomalies (Fig. 6h). Note that, due to the poleward migration of the KE jet (recall Fig. 5b), the
360 dashed box in Fig. 6h is shifted 1° northward in latitude relative to that in Fig. 6d to more
361 accurately capture the interior wind forcing relevant to the newly-established KE dynamic
362 state. From the perspective of KE–atmosphere coupling, this change in W_{ek} suggests that a
363 *positive feedback mechanism* may now be operating, reinforcing the persistence of the stable
364 KE state. Although we do not pursue this issue further here, it will be important for future

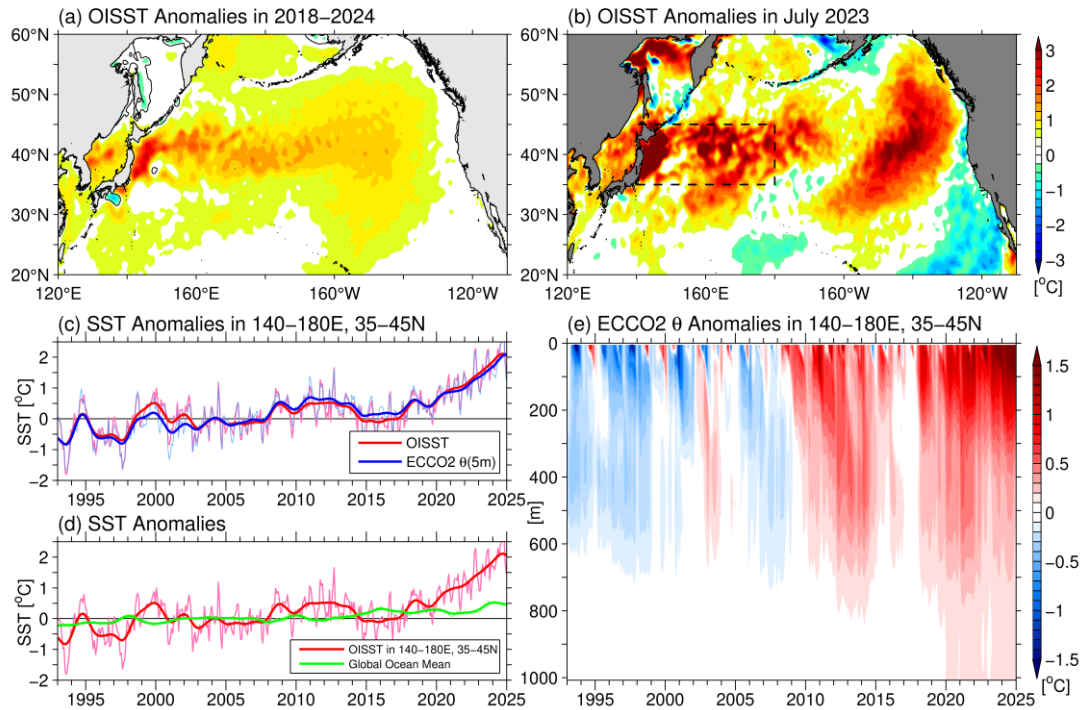
365 studies to examine how this altered atmospheric response might contribute to the sustained,
366 highly stable KE dynamic regime observed after 2018.

367 **5. Upper ocean temperature budget**

368 The dynamic regime change in the Kuroshio/KE has exerted a significant influence on
369 upper ocean thermal conditions across the midlatitude North Pacific. Figure 7a shows the SST
370 anomaly map for 2018–2024 relative to the 1993–2017 mean, based on the OI-SST dataset. A
371 prominent basin-scale warming is evident, centered along the boundary between the
372 subtropical and subpolar gyres. Although the warming appears continuous across the basin,
373 closer examination reveals distinct spatial and temporal characteristics between the western
374 and eastern sectors. As illustrated in the July 2023 SST anomaly map (Fig. 7b), warm SST
375 anomalies in the western basin are largely confined to the 35°–45°N band, extending from the
376 Japanese coast to the dateline. This band coincides with regions of elevated SSH and eddy
377 kinetic energy following the 2018 Kuroshio/KE regime shift (see Figs. 1b and 5b). Notably,
378 SST anomalies exceeding 4°C are observed along the east coast of Japan, indicating intense
379 regional warming. The oceanic and atmospheric impacts of this extreme warming have been
380 examined in several recent studies (Sato et al. 2024; Kawai et al. 2024; Sugimoto et al. 2025;
381 Hirata et al. 2025a). In contrast, SST anomalies east of the dateline display a broader meridional
382 structure (Fig. 7b), a pattern also evident in the long-term anomaly map in Fig. 7a. Given the
383 scope of this study, our analysis will focus on the SST warming in the northwestern Pacific
384 basin, where the connection to the Kuroshio/KE dynamic regime change is most direct.

385 The red curve in Fig. 7c shows the SST anomaly timeseries averaged over the 140°E–180°,
386 35°–45°N region (dashed box in Fig. 7b). While a modest warming tendency of 0.025°C/yr is
387 evident prior to 2018, the post-2018 period exhibits a tenfold increase in the warming rate,
388 reaching 0.265°C/yr. To place this regional warming in a broader context, Fig. 7d compares
389 the SST anomalies in the 140°E–180°, 35°–45°N region with the global mean SST anomaly
390 timeseries (green line), which serves as a proxy for anthropogenic forcing. The global mean
391 SST increase is significantly weaker than the regional warming observed in the western North
392 Pacific, suggesting that the latter is predominantly driven by internal ocean-atmosphere
393 variability rather than by global anthropogenic forcing.

394 To assess the vertical reach of this warming signal, we also examine the ECCO2 ocean
395 state estimate. The ECCO2-derived SST anomalies for the same region are shown by the blue



396

397 Fig. 7. (a) SST anomalies in the North Pacific Ocean during 2018–2024, based on the OI-SST product.
 398 (b) Same as (a), but for July 2023. The dashed box denotes the region 140°E–180°, 35°–45°N. (c) SST
 399 anomaly timeseries averaged within the dashed line in (b), from the OI-SST (red curves) and ECCO2
 400 (blue curves). Thin lines represent monthly anomalies; thick lines indicate low-pass filtered anomalies.
 401 (d) Same as (c), with the green line showing the global mean SST variations, based on NOAA National
 402 Centers for Environmental Information. (e) Temperature anomalies as a function of time and depth,
 403 averaged in the 140°E–180°, 35°–45°N box, based on ECCO2 product. All temperature anomalies here
 404 are relative to the 1993–2017 mean.

405 curve in Fig. 7c, which agrees closely with the OI-SST time series, confirming the reliability
 406 of ECCO2 for vertical structure analysis. Figure 7e shows temperature anomalies as a function
 407 of time and depth in the same region, based on ECCO2 output. Notably, the warming anomalies
 408 observed in the SST fields (Figs. 7a–7b) are not confined to the surface mixed layer but extend
 409 down to the main thermocline. This vertical penetration of warming (see also Minobe 2025;
 410 Trenberth et al. 2025) suggests that in addition to surface heat fluxes, subsurface oceanic
 411 processes, such as those linked to changes in the KE dynamic state, have contributed
 412 significantly to the anomalous upper-ocean warming in the western North Pacific.

413 To quantify the relative contributions of dynamic versus thermodynamic processes to
 414 upper-ocean warming, we follow the methodology of Qiu et al. (2017) and perform a

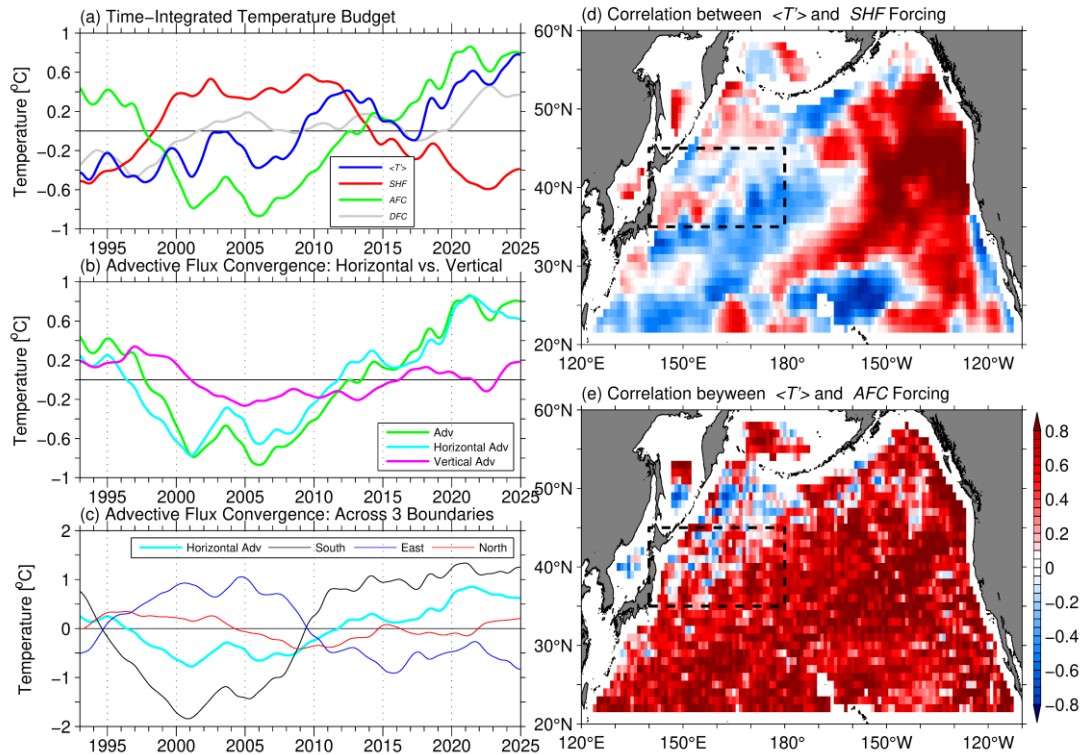
415 temperature budget analysis using the ECCO2 ocean state estimate. The governing equation
 416 for the upper-ocean temperature anomalies T' , averaged over a layer of depth H , is given by:

$$417 \quad \frac{\partial}{\partial t} \langle T' \rangle = -\frac{1}{H} \int_{-H}^0 (\mathbf{u} \cdot \nabla T)' dz + \frac{Q'_{net}}{\rho_0 C_p H} + \left(\frac{K_h}{H} \int_{-H}^0 \nabla_h^2 T' dz - \frac{K_z}{H} \frac{\partial T'}{\partial z} \Big|_{z=-H} \right), \quad (3)$$

418 where $\langle T' \rangle = \frac{1}{H} \int_{-H}^0 T' dz$ represents the depth-averaged temperature anomaly, $\mathbf{u} = (u, v, w)$
 419 is the 3D velocity vector, Q'_{net} is the net surface heat flux anomaly, C_p is the specific heat of
 420 seawater, and K_h and K_z are the horizontal and vertical eddy diffusivities, respectively. All
 421 anomalies are defined relative to the 1993–2024 mean, the analysis period for this study.
 422 Physically, the first term on the right-hand side of Eq. (3) represents the advective flux
 423 convergence (*AFC*) contribution, the second term represents the surface heat flux (*SHF*)
 424 contribution, and the final term accounts for eddy diffusive flux convergence (*DFC*). Based on
 425 the vertical structure of the temperature anomalies shown in Fig. 7e, we set $H = 400\text{m}$ for our
 426 analysis. Tests with other depth values confirm that the qualitative results remain robust.

427 Figure 8a shows the time-integrated contributions of the individual terms in Eq. (3),
 428 averaged over the $140^\circ\text{--}180^\circ\text{E}$, $35^\circ\text{--}45^\circ\text{N}$ region. Owing to the vertical coherence of the
 429 temperature anomalies within the upper 400 m, the timeseries of the box-averaged $\langle T' \rangle$
 430 (blue line) closely track the SST anomaly timeseries shown in Fig. 7c. Overall, there exists a
 431 strong *negative* correlation between the *SHF* term and the *AFC* term (red and green lines,
 432 respectively), indicating that surface heat flux forcing tends to oppose the effects of ocean
 433 advection in driving upper-ocean temperature changes. In comparison, the *DFC* term (gray
 434 line) contributes less to the total temperature tendency. Following the Kuroshio/KE regime
 435 change in 2018, the increase in $\langle T' \rangle$ was driven primarily by the *AFC* term, with a secondary
 436 contribution from the *DFC* term. In contrast, the *SHF* term exerted a damping effect, acting to
 437 offset the upper-ocean warming induced by dynamic oceanic processes. Notice that the Q'_{net}
 438 signal in the *SHF* term is predominantly controlled by turbulent heat flux anomalies, and shows
 439 little correlation with net shortwave flux (not shown).

440 That the *SHF* forcing works to damp the upper ocean temperature anomalies generated by
 441 oceanic processes is confirmed by the local correlation maps between the $\langle T' \rangle$ timeseries
 442 and the time-integrated *SHF* and *AFC* forcings, shown in Figs. 8d and 8e, respectively. Across
 443 much of the western North Pacific basin, these maps reveal that upper ocean temperature
 444 anomalies are primarily driven by oceanic advective and subsequently damped by SHF forcing.
 445 In fact, the spatial pattern in Fig. 8d closely resembles the observed surface eddy kinetic energy



446

447 Fig. 8. (a) Time-integrated upper ocean temperature budget terms averaged over the 140°E–180°,
 448 35°–45°N region, based on the ECCO2 ocean state estimate. Blue line denotes the evolution of the
 449 vertically averaged temperature anomaly $\langle T' \rangle$; red, green, and grey lines represent contributions
 450 from the *SHF*, *AFC*, *DFC* terms, respectively. The time mean of each term has been individually
 451 removed. (b) Decomposition of the *AFC* term (green line in panel a) into horizontal (teal) and vertical
 452 (pink) advective component. (c) Breakdown of the horizontal *AFC* component (teal line in panel b) into
 453 contributions across the southern (black), eastern (blue), and northern (red) boundaries of the analysis
 454 box. (d) Spatial map of the correlation coefficient between $\langle T' \rangle$ changes and *SHF* forcing across the
 455 North Pacific. (e) Same as (d), but for the correlation between $\langle T' \rangle$ changes and *AFC* forcing.

456 distribution (e.g., Fig. 1 in Qiu et al. 2022): regions with elevated eddy activity exhibit strong
 457 negative correlations between $\langle T' \rangle$ and *SHF* forcing. This indicates that *SHF* forcing tends
 458 to counteract the upper ocean temperature anomalies induced by oceanic eddy variability.

459 To better understand the nature of the *AFC* forcing averaged over the 140°–180°E,
 460 35°–45°N region, it is useful to separate its contributions into horizontal and vertical
 461 components. As shown in Fig. 8b, the total *AFC* term (green line) is largely governed by its
 462 horizontal component (teal line). This indicates that the advective temperature flux
 463 convergence is primarily controlled by variations in horizontal upper-ocean circulation, rather
 464 than by vertical processes such as Ekman pumping. To further isolate the horizontal

465 contributions, we decompose the advective fluxes through the southern, eastern, and northern
466 boundaries of the analysis box (note that the western boundary is effectively closed by the
467 Japanese landmass). Figure 8c shows that changes in the horizontal *AFC* forcing are primarily
468 imposed by heat flux convergence through the southern boundary (black line), partially offset
469 by heat export through the eastern boundary (blue line). The flux through the northern boundary
470 (red line) plays only a minor role. Physically, this suggests that the upper ocean temperature
471 anomalies observed in the 35°–45°N band of the western North Pacific (Fig. 7) are mainly
472 driven by lateral heat input from the poleward-migrating KE jet across the southern boundary
473 near 35°N, with a portion of this heat subsequently advected eastward into the central and
474 eastern North Pacific.

475 In contrast to the dominant forcing mechanisms identified in the western basin, Figs. 8d
476 and 8e suggest that the upper ocean temperature anomalies in the eastern North Pacific (recall
477 the basin-wide SST warming shown in Fig. 7b) are likely governed by a combination of *SHF*
478 and *AFC* forcings. For the *AFC* component in this region, it is plausible that wind-driven
479 Ekman transport convergence, rather than geostrophic flow convergence, plays a more
480 influential role in driving upper ocean warming. This distinction highlights the differing
481 dynamics and thermodynamics operating across the basin. To further elucidate the processes
482 underlying the observed warming in the eastern North Pacific, it would be worthwhile for
483 future studies to carry out an upper ocean temperature budget analysis similar to that presented
484 in Figs. 7 and 8, with a dedicated focus on the mechanisms active in the eastern basin.

485 **6. Summary**

486 The Kuroshio and Kuroshio Extension (KE) form a nonlinearly interacting western
487 boundary current system within the wind-driven subtropical gyre of the North Pacific Ocean.
488 By releasing spatio-temporally varying heat and moisture to the overlying midlatitude
489 atmosphere, this current system acts as a heat engine that drives low-frequency climate
490 variability across the North Pacific. Following the 1976/77 North Pacific climate regime shift,
491 the KE system east of Japan entered a quasi-regular oscillation between stable and unstable
492 dynamic states. The oscillation had a decadal timescale and was regulated by a delayed
493 negative feedback loop involving interactions between the KE jet and extratropical storm tracks
494 spanning the North Pacific basin. During this regime from 1976/77 to early 2017, the upstream
495 Kuroshio south of Japan underwent five large meander (LM) events but otherwise remained in

496 a non-large meander path configuration. Its dynamical linkage to the downstream quasi-
497 decadal KE variability remained relatively weak throughout this time.

498 A significant regime shift occurred in the Kuroshio/KE system in late 2017. Since 2018
499 and persisting through the past seven years, the Kuroshio south of Japan became locked in a
500 persistent LM state, while the KE transitioned into an exceptionally stable dynamic state. This
501 newly established Kuroshio/KE configuration is unprecedented in the past 75 years, during
502 which reliable reanalysis and ocean model simulation data are available. In this study, we have
503 identified three processes likely responsible for this unique dynamic state. First, the wind
504 forcing over the subtropical North Pacific has exhibited an unusually persistent dipolar pattern
505 since 2018, characterized by weakened winds over the southern subtropical gyre (20°–32°N)
506 and strengthened winds over the northern subtropical gyre (32°–45°N). This anomalous wind
507 pattern favors a weakened wind-driven Kuroshio transport in the south — conducive to
508 maintaining the LM path — and a strengthened Sverdrup transport in the north, which shifts the
509 KE jet poleward. Second, once this new dynamic regime is established, nonlinear interactions
510 between the Kuroshio and KE systems can help sustain it. Specifically, the presence of the LM
511 path steers the upstream KE jet northeastward, while the poleward-shifted KE jet reduces the
512 westward-propagating mesoscale disturbances that typically destabilize the LM, thereby
513 creating a mutually reinforcing configuration. Third, the atmospheric response to the stable KE
514 dynamic state after 2018 appears to differ subtly from that of the pre-2018 period. Previously,
515 a positive wind stress curl anomaly commonly emerged in the 31°–36°N band of the eastern
516 North Pacific during stable KE phases. After 2018, however, this pattern has been replaced by
517 a negative wind stress curl anomaly. This anomalous forcing can enhance positive SSH
518 anomalies via oceanic adjustment processes, reinforcing the existing stable KE configuration
519 and potentially establishing a positive feedback loop.

520 An important manifestation of the new Kuroshio/KE dynamic state is the progressive
521 poleward migration by the KE jet and its associated mesoscale eddy activity. This poleward
522 shift has had a pronounced impact on the thermal structure of the upper ocean in the western
523 North Pacific. Since 2018, the upper 400 meters of the ocean in the 35°–45°N band have
524 undergone steady warming, with the SST increasing at a rate of 0.265°C/yr and the vertically
525 averaged temperature over the 0–400 m layer warming at 0.086°C/yr. An upper ocean
526 temperature budget analysis based on the ECCO2 ocean state estimate reveals that this
527 warming is driven primarily by lateral advective temperature fluxes entering through the

528 southern boundary at 35°N, and secondarily by lateral outflow through the eastern boundary
529 and vertical diffusive processes. In contrast, the net surface heat flux has acted as a damping
530 mechanism, offsetting part of the warming induced by oceanic advection.

531 The newly-established Kuroshio/KE dynamic state is an ongoing phenomenon. Many of
532 the conclusions drawn in this study, particularly regarding the three processes proposed to
533 sustain the new dynamic regime, are based on available observational evidence of the past
534 seven years (2018–2024). To advance our understanding, future observational and modeling
535 studies will be essential to validate and refine these findings, as well as to assess the extent to
536 which the evolution of the Kuroshio/KE dynamic state can be predicted.

537

538 *Acknowledgments.*

539 This study was supported by NSF OCE-2445946 and NASA Ocean Surface Topography
540 Science Team (OSTST) Award 80NSSC21K1186. We gratefully acknowledge the insightful
541 reviews provided by three anonymous reviewers, as well as valuable discussions with Shoshiro
542 Minobe, Eitarou Oka, and Niklas Scheider.

543

544 *Data Availability Statement.*

545 The Level-4 DUACS SSH dataset is available at <https://doi.org/10.48670/moi-00148>. The
546 ECMWF ERA-5 reanalysis product is available at
547 <https://www.ecmwf.int/en/forecasts/dataset/ecmwf-reanalysis-v5>. The ECCO2 ocean state
548 estimate product is available at https://apdrc.soest.hawaii.edu/datadoc/ecco2_cube92.php. The
549 optimum interpolation SST data is available at [https://www.ncei.noaa.gov/products/climate-](https://www.ncei.noaa.gov/products/climate-data-records/sea-surface-temperature-optimum-interpolation)
550 [data-records/sea-surface-temperature-optimum-interpolation](https://www.ncei.noaa.gov/products/climate-data-records/sea-surface-temperature-optimum-interpolation), and the global mean SST data is
551 available at [https://www.ncei.noaa.gov/access/monitoring/climate-at-a-glance/global/time-](https://www.ncei.noaa.gov/access/monitoring/climate-at-a-glance/global/time-series/globe/tavg/ocean/1/0/1850-2025)
552 [series/globe/tavg/ocean/1/0/1850-2025](https://www.ncei.noaa.gov/access/monitoring/climate-at-a-glance/global/time-series/globe/tavg/ocean/1/0/1850-2025).

553

554

REFERENCES

- 555 Ceballos, L., E. Di Lorenzo, C. D. Hoyos, N. Schneider, and B. Taguchi, 2009: North Pacific
556 Gyre Oscillation synchronizes climate variability in the eastern and western boundary
557 current systems. *J. Climate*, **22**, 5163-5174.
- 558 Chang, Y.-L., K. Morita, K. Muramatsu, O. Kishida, and M. Kuroki, 2025: Northern shifts in
559 the migration of Japanese glass eels to subarctic Hokkaido Island over the past three
560 decades. *Ocean Dyn.*, **75**, 10, <https://doi.org/10.1007/s10236-024-01651-6>.
- 561 Deser, C., R.A. Tomas, and S. Peng, 2007: The transient atmospheric circulation response to
562 North Atlantic SST and sea ice anomalies. *J. Climate*, **20**, 4751-4767.
- 563 Fan, M., X. Liu, T. Liu, and D. Chen, 2025: The role of local wind stress curl in modulating
564 Kuroshio Extension latitudinal variability. *J. Geophys. Res.*, **130**, e2024JC021742.
565 <https://doi.org/10.1029/2024JC021742>.
- 566 Ferreira, D., and C. Frankignoul, 2005: The transient atmospheric response to midlatitude SST
567 anomalies. *J. Climate*, **18**, 1049-1067.
- 568 Frankignoul, C., N. Sennechael, Y.-O. Kwon, and M. A. Alexander, 2011: Influence of the
569 meridional shifts of the Kuroshio and the Oyashio Extensions on the atmospheric
570 circulation. *J. Climate*, **24**, 762-777.
- 571 Gan, B., T. Wang, L. Wu, J. Li, B. Qiu, H. Yang, and L. Zhang, 2023: A mesoscale ocean-
572 atmosphere coupled pathway for decadal variability of the Kuroshio Extension system. *J.*
573 *Climate*, **36**, 485-510.
- 574 Hersbach, H., and Co-authors, 2020: The ERA5 global reanalysis. *Quart. J. Royal Meteorol.*
575 *Soc.*, **146**, 1999–2049. <https://doi.org/10.1002/qj.3803>.
- 576 Hirata, H., R. Kawamura, and M. Nonaka, 2025a: Effects of a marine heatwave associated with
577 the Kuroshio Extension large meander on extreme precipitation in September 2023. *Sci.*
578 *Reports*, **15**, 5332, <https://doi.org/10.1038/s41598-025-88294-9>.
- 579 Hirata, H., H. Nishikawa, N. Usui, T. Miyama, S. Sugimoto, A. Kusaka, and T. Seto, 2025b:
580 The Kuroshio large meander and its various impacts: a review. *J. Oceanogr.*, **81**, 165-185.
581 <https://doi.org/10.1007/s10872-025-00753-z>.

582 Huang, B., C. Liu, V. Banzon, E. Freeman, G. Graham, B. Hankins, T. Smith, H.-M. Zhang,
583 2021: Improvements of the daily optimum interpolation sea surface temperature (DOISST)
584 version 2.1. *J. Climate*, **34**, 2923–2939.

585 Imawaki, S., A.S. Bower, L. Beal, and B. Qiu, 2013: *Western Boundary Currents*. In Ocean
586 Circulation and Climate - A 21st Century Perspective, 2nd Edition, G. Siedler, S.M.
587 Griffies, W.J. Gould and J. Church (eds.); Academic Press, pp.305-338.

588 Joh, Y., and E. Di Lorenzo, 2019: Interactions between Kuroshio Extension and Central
589 Tropical Pacific lead to preferred decadal timescale oscillations in Pacific climate. *Sci.*
590 *Report*, **9**, 13558, <https://doi.org/10.1038/s41598-019-49927-y>.

591 Joh, Y., and Co-authors, 2022: Seasonal-to-decadal variability and prediction of the Kuroshio
592 Extension in the GFDL coupled ensemble reanalysis and forecasting system. *J. Climate*,
593 **35**, 3515–3535.

594 Jousset, S., S. Mulet, J. Wilkin, E. Greiner, G. Dibarboure, and N. Picot, 2022: New global
595 mean dynamic topography CNES-CLS-22 combining drifters, hydrological profiles and
596 high frequency radar data", OSTST, <https://doi.org/10.24400/527896/a03-2022.3292>.

597 Kawakami, Y., H. Nakano, L. S. Urakawa, T. Toyoda, K. Aoki, and N. Usui, 2023: Northward
598 shift of the Kuroshio Extension during 1993–2021. *Sci. Report*, **13**, 16223,
599 <https://doi.org/10.1038/s41598-023-43009-w>.

600 Kawai, Y., E. Oka, K. Sato, S. Hosoda, S. Kido, 2024: Marine heatwave in the Oyashio region
601 in 2022/23 and its impact on subsurface dissolved oxygen. *J. Oceanogr.*, **80**,
602 <https://doi.org/10.1007/s10872-024-00731-x>.

603 Kelly, K.A., R.J. Small, R. M. Samelson, B. Qiu, T. M. Joyce, Y.-O. Kwon, and M.F. Cronin, 2010:
604 Western boundary currents and frontal air-sea interaction: Gulf Stream and Kuroshio Extension.
605 *J. Climate*, **23**, 5644-5667.

606 Kwon, Y.-O., and T. M. Joyce, 2013: Northern Hemisphere winter atmospheric transient eddy heat
607 fluxes and the Gulf Stream and Kuroshio-Oyashio Extension variability. *J. Climate*, **26**, 9839-
608 9859.

609 Lizarbe Barreto, D. A., R. Chevarria Saravia, T. Nagai, and T. Hirata, 2021: Phytoplankton
610 increase along the Kuroshio due to the Large Meander. *Front. Mar. Sci.*, **8**.
611 <https://www.frontiersin.org/articles/10.3389/fmars.2021.677632>.

612 Ma, X., J. Zhao, P. Chang, X. Liu, R. Montuoro, R.J. Small, F.O. Bryan, R.J. Greatbatch, P.
613 Brandt, D. Wu, X. Lin, and L. Wu, 2016: Western boundary currents regulated by
614 interaction between ocean eddies and the atmosphere. *Nature*, **535**, 533-537.

615 Mantua, N. J., and S. R. Hare, 2002: The Pacific decadal oscillation. *J. Oceanogr.*, **58**, 35–44.
616 <http://doi.org/10.1023/A:1015820616384>.

617 Mantua, N. J., S. R. Hare, Y. Zhang, J. M. Wallace, and R. C. Francis, 1997: A Pacific
618 interdecadal climate oscillation with impacts on salmon production. *Bull. Ame. Meteor.*
619 *Soc.*, **78**, 1069–1079. <http://doi.org/10.1175/1520-0477>.

620 Menemenlis, D., and Co-Authors, 2008: ECCO2: High resolution global ocean and sea ice data
621 synthesis. *Mercator Ocean Quarterly Newsletter*, **31**, 13-21.

622 Miller, A., D. Cayan, T. Barnett, N. Graham, and J. Oberhuber, 1994: The 1976–77 climate
623 shift of the Pacific Ocean. *Oceanography*, **7**, 21–26.
624 <http://doi.org/10.5670/oceanog.1994.11>.

625 Minobe, S., 1997: A 50–70 year climatic oscillation over the North Pacific and North America.
626 *Geophys. Res. Lett.*, **24**, 683–686.

627 Minobe, S., 2025: Exceptional heat and basin-scale connections in the Kuroshio-Oyashio
628 region in the early 2020s. *J. Oceanogr.*, **81**. <https://doi.org/10.21203/rs.3.rs-5465083/v1>.

629 Mizuno, K., and W.B. White, 1983: Annual and interannual variability in the Kuroshio Current
630 system. *J. Phys. Oceanogr.*, **13**, 1847-1867.

631 Nakamura, H., T. Sampe, Y. Tanimoto, and A. Shimpo, 2004: Observed associations among
632 storm tracks, jet streams and midlatitude oceanic fronts. *Earth's Climate: The Ocean-*
633 *Atmosphere Interaction*. Geophys. Monogr., **147**, Amer. Geophys. Union, 329-346.

634 Nishikawa, H., E. Oka, and S. Sugimoto, 2023: Subtropical Mode Water in a recent persisting
635 Kuroshio large-meander period: Part II – formation and temporal evolution in the Kuroshio
636 recirculation gyre off Shikoku. *J. Oceanogr.*, **79**, 461-471. [https://doi.org/10.1007/s10872-](https://doi.org/10.1007/s10872-023-00689-2)
637 [023-00689-2](https://doi.org/10.1007/s10872-023-00689-2).

638 Nonaka, M., H. Sasaki, M. Taguchi, and N. Schneider, 2020: Atmospheric-driven and intrinsic
639 interannual-to-decadal variability in the Kuroshio Extension jet and eddy activities. *Front.*
640 *Mar. Sci.*, **7**, 547442. <https://doi.org/10.3389/fmars.2020.547442>.

641 Oka, E., H. Nishikawa, S. Sugimoto, B. Qiu, and N. Schneider, 2021: Subtropical mode water
642 in a recent persisting Kuroshio large-meander period: part I -- formation and advection over
643 the entire distribution. *J. Oceanogr.*, **77**, 781-795.

644 Oka, E., S. Sugimoto, F. Kobashi, H. Nishikawa, S. Kanada, T. Nasuno, R. Kawamura, and M.
645 Nonaka, 2023: Subtropical Mode Water south of Japan impacts typhoon intensity. *Sci.*
646 *Adv.*, **9**, <https://doi.org/10.1126/sciadv.adi2793>.

647 Okajima, S., and Co-authors, 2018: Mechanisms for the maintenance of the wintertime basin-
648 scale atmospheric response to decadal SST variability in the North Pacific Subarctic Frontal
649 Zone. *J. Climate*, **31**, 297-315.

650 Pierini, S., 2014: Kuroshio Extension bimodality and the North Pacific Oscillation: A case of
651 intrinsic variability paced by external forcing. *J. Climate*, **27**, 448-454.

652 Qiu, B., 2019: *Kuroshio and Oyashio Currents*. Encyclopedia of Ocean Sciences (3rd Edn.),
653 edited by J.K. Cochran, H. Bokuniewicz, P. Yager. Academic Press, 384-394.

654 Qiu, B., and S. Chen, 2005: Variability of the Kuroshio Extension jet, recirculation gyre and
655 mesoscale eddies on decadal timescales. *J. Phys. Oceanogr.*, **35**, 2090-2103.

656 Qiu, B., and S. Chen, 2010: Eddy-mean flow interaction in the decadal-modulating Kuroshio
657 Extension system. *Deep-Sea Res. II*, **57**, 1098-1110.

658 Qiu, B., and S. Chen, 2021: Revisit of the occurrence of the Kuroshio large meander south of
659 Japan. *J. Phys. Oceanogr.*, **51**, 3679-3694.

660 Qiu, B., S. Chen, and N. Schneider, 2017: Dynamical links between the decadal variability of
661 the Oyashio and Kuroshio Extensions. *J. Climate*, **30**, 9591-9605.

662 Qiu, B., S. Chen, N. Schneider, and B. Taguchi, 2014: A coupled decadal prediction of the
663 dynamic state of the Kuroshio Extension system. *J. Climate*, **27**, 1751-1764.

664 Qiu, B., S. Chen, N. Schneider, E. Oka, and S. Sugimoto, 2020: On reset of the wind-forced
665 decadal Kuroshio Extension variability in late 2017. *J. Climate*, **33**, 10813-10828.

666 Qiu, B., T. Nakano, S. Chen, and P. Klein, 2022: Bi-directional energy cascades in the Pacific
667 Ocean from equator to subarctic gyre. *Geophys. Res. Lett.*, **49**, e2022GL097713.

668 Qiu, B., S. Chen, and E. Oka, 2023: Why did the 2017 Kuroshio Large Meander become the
669 longest in the past 70 years? *Geophys. Res. Lett.*, **50**, e2023GL103548. [https://doi.](https://doi.org/10.1029/2023GL103548)
670 [org/10.1029/2023GL103548](https://doi.org/10.1029/2023GL103548).

671 Revelard, A., C. Frankignoul, N. Sennechael, Y.-O. Kwon, and B. Qiu, 2016: Influence of the
672 decadal variability of the Kuroshio Extension on the atmospheric circulation in the cold
673 season. *J. Climate*, **29**, 2123-2144.

674 Sasaki, Y. N., R. Ito, 2024: Impact of the Kuroshio large meander on local atmospheric
675 circulation and precipitation in winter. *Prog. Earth Planet Sci.*, **11**,
676 <https://doi.org/10.1186/s40645-024-00620-3>.

677 Sasaki, Y. N., S. Minobe, and N. Schneider, 2013: Decadal response of the Kuroshio Extension
678 jet to Rossby waves: Observation and thin-jet theory. *J. Phys. Oceanogr.*, **43**, 442-456.

679 Sato, H., K. Takemura, A. Ito, T. Umeda, S. Maeda, Y. Tanimoto, M. Nonaka, H. Nakamura,
680 2024: Impact of an unprecedented marine heatwave on extremely hot summer over
681 Northern Japan in 2023. *Sci. Report*, **14**, 16100. [https://doi.org/10.1038/s41598-024-](https://doi.org/10.1038/s41598-024-65291-y)
682 [65291-y](https://doi.org/10.1038/s41598-024-65291-y).

683 Small, R.J., R.A. Tomas, F.O. Bryan, 2014: Storm track response to ocean fronts in a global
684 high-resolution climate model. *Climate Dyn.*, **43**, 805-828.

685 Smirnov, D., M. Newman, M.A. Alexander, Y.-O. Kwon, and C. Frankignoul, 2015:
686 Investigating the local atmospheric response to a realistic shift in the Oyashio sea surface
687 temperature front. *J. Climate*, **28**, 1126-1147.

688 Sugimoto, S., and K. Hanawa, 2012: Relationship between the path of the Kuroshio in the south
689 of Japan and the path of the Kuroshio Extension in the east. *J. Oceanogr.*, **68**, 219-225.

690 Sugimoto, S., B. Qiu, and M. Omori, 2020: Marked coastal warming off Tokai attributable to
691 Kuroshio large meander. *J. Oceanogr.*, **76**, 141-154.

692 Sugimoto, S., B. Qiu, and N. Schneider, 2021: Local atmospheric response to the Kuroshio
693 Large Meander path in summer and its remote influence on the climate of Japan. *J. Climate*,
694 **34**, 3571-3589.

695 Sugimoto, S., A. Kojima, T. Sakamoto, Y. Kawakami, and H. Nakano, 2025: Influence of
696 extreme northward meandered Kuroshio Extension during 2023–2024 on ocean–
697 atmosphere conditions in the Sanriku offshore region, Japan. *J. Oceanogr.*, **81**,
698 <https://doi.org/10.1007/s10872-025-00747-x>.

- 699 Taguchi, B., S.-P. Xie, N. Schneider, M. Nonaka, H. Sasaki, and Y. Sasai, 2007: Decadal
700 variability of the Kuroshio Extension: observations and an eddy-resolving model hindcast.
701 *J. Climate*, **20**, 2357-2377.
- 702 Taguchi, B., H. Nakamura, M. Nonaka, N. Komori, A. Kuwano-Yoshida, K. Takaya, and A.
703 Goto, 2012: Seasonal evolutions of atmospheric response to decadal SST anomalies in the
704 North Pacific subarctic frontal zone: Observations and a coupled model simulation. *J.*
705 *Climate*, **25**, 111-139.
- 706 Tamura, Y., and T. Tozuka, 2023: Dominant forcing regions of decadal variations in the
707 Kuroshio Extension revealed by a linear Rossby wave model. *Geophys. Res. Letts.*, **50**,
708 e2023GL102995. <https://doi.org/10.1029/2023GL102995>.
- 709 Trenberth, K. E., L. Cheng, Y. Pan, J. Fasullo, and M. Mayer, 2025: Distinctive pattern of
710 global warming in ocean heat content. *J. Climate*, **38**, 2155-2168.
- 711 Usui, N., H. Tsujino, H. Nakano, and S. Matsumoto, 2013: Long-term variability of the
712 Kuroshio path south of Japan. *J. Oceanogr.*, **69**, 647–670.
- 713 White, W. B., and J. P. McCreary, 1976: On the formation of the Kuroshio meander and its
714 relationship to the large-scale ocean circulation. *Deep-Sea Res.*, **23**, 33–47.
- 715 Wilson, C., B. Sinha, and R.G. Williams, 2009: The effect of ocean dynamics and orography
716 on atmospheric storm tracks. *J. Climate*, **22**, 3689-3702.
- 717 Wunsch, C., P. Heimbach, R. Ponte, and I. Fukumori, 2009: The global general circulation of
718 the ocean estimated from the ECCO-consortium. *Oceanography*, **22**, 88–103,
719 doi:10.5670/oceanog.2009.41.